

**Atomic Layer Deposition on Porous Substrates
From General Formulation to Fibrous Substrates and Scaling Laws**

Szmyt, Wojciech; Guerra-Nuñez, Carlos; Huber, Lukas; Dransfeld, Clemens; Utke, Ivo

DOI

[10.1021/acs.chemmater.1c03164](https://doi.org/10.1021/acs.chemmater.1c03164)

Publication date

2021

Document Version

Accepted author manuscript

Published in

Chemistry of Materials

Citation (APA)

Szmyt, W., Guerra-Nuñez, C., Huber, L., Dransfeld, C., & Utke, I. (2021). Atomic Layer Deposition on Porous Substrates: From General Formulation to Fibrous Substrates and Scaling Laws. *Chemistry of Materials*, 34(1), 203-216. <https://doi.org/10.1021/acs.chemmater.1c03164>

Important note

To cite this publication, please use the final published version (if applicable).
Please check the document version above.

Copyright

Other than for strictly personal use, it is not permitted to download, forward or distribute the text or part of it, without the consent of the author(s) and/or copyright holder(s), unless the work is under an open content license such as Creative Commons.

Takedown policy

Please contact us and provide details if you believe this document breaches copyrights.
We will remove access to the work immediately and investigate your claim.

Atomic layer deposition on porous substrates: from general formulation to fibrous substrates and scaling laws.

Wojciech Szmyt^{*,†,‡,§,⊥,0}, Carlos Guerra-Nuñez^{||}, Lukas Huber[◇], Clemens Dransfeld[▽] and Ivo Utke^{||}

[†] Institute of Polymer Engineering, FHNW University of Applied Sciences and Arts Northwestern Switzerland, Klosterzelgstrasse 2, CH 5210 Windisch, Switzerland

[‡] Laboratory for Micro- and Nanotechnology, Paul Scherrer Institute, CH 5232 Villigen PSI, Switzerland

[§] Department of Physics, University of Basel, Klingelbergstrasse 82, CH 4056 Basel, Switzerland

[⊥] Swiss Nanoscience Institute, University of Basel, Klingelbergstrasse 82, CH 4056 Basel, Switzerland

^{||} Laboratory for Mechanics of Materials and Nanostructures, EMPA Swiss Federal Laboratories for Materials Science and Technology, Feuerwerkerstrasse 39, CH 3602 Thun, Switzerland

[◇] Building Energy Materials and Components, EMPA Swiss Federal Laboratories for Materials Science and Technology, Überlandstrasse 129, CH 8600 Dübendorf, Switzerland

[▽] Aerospace Manufacturing Technologies, Delft University of Technology, Kluyverweg 1, 2629 HS Delft, The Netherlands

ABSTRACT: Atomic Layer Deposition (ALD) is a technique of choice for uniform, conformal coating of substrates of complex geometries, owed to its characteristic self-limiting surface reactions upon sequential exposure to precursor vapors. In order to achieve the uniform coating, a sufficient gas exposure needs to be provided. This requirement becomes particularly relevant for highly porous and high aspect-ratio substrates, where the gas transport into the substrate structure is limited by diffusion (diffusion-limited regime), or for ALD precursor systems exhibiting low surface reaction rate (reaction-limited regime). This work reports how the distinction between diffusion- and reaction-limited ALD regimes is directly quantitatively related to the width of the reaction front and the profile of chemisorption coverage in a single cycle ALD, all of them being determined by the natural length unit of the system. We introduce a new parametrization of the system based on its natural system of units, dictated by the scales of the physical phenomena governing the process. We present a range of scaling laws valid for a general porous substrate, which scale intuitively with the natural units of the system. The scaling laws describe (i) the coating depth in a diffusion-limited regime with respect to the gas exposure, (ii) the chemisorption coverage in a reaction-limited regime with respect to the gas exposure, and (iii) the width of the reaction zone in the diffusion-limited regime. For the first time, the distinction between diffusion- and reaction-limited ALD regimes is directly quantitatively related to the width of the reaction zone and the profile of chemisorption coverage in a single cycle ALD. The model system for the multicycle diffusion-limited coating of random fibrous mats was validated with an experiment of ALD on forest of tortuous carbon nanotubes (CNTs).

List of symbols

Latin:	h	layer thickness increment in a single ALD cycle
A	h_T	Thiele number
D	J	classical gas impingement rate
d	J_{wall}	gas impingement rate onto walls of porous nanostructure
d_{aux}	k	proportionality constant relating d_{aux} and z
d_{m}	k_B	Boltzmann's constant
d_{max}	Kn	Knudsen number
d_{min}	l	thickness of the porous structure
d_{N_2}	n	precursor gas concentration
d_{TMA}	\bar{n}	precursor gas concentration, dimensionless
	n_0	precursor gas concentration unit
	N_A	Avogadro's constant

N_{cyc}	number of ALD cycles
N_d	number of diameter measurements
n_R	precursor concentration in ALD reactor over sample
\bar{n}_R	precursor concentration in ALD reactor over sample, dimensionless
p	precursor pressure
P/P_0	relative pressure in Brunauer–Emmett–Teller (BET) surface area measurement
p_{N_2}	partial pressure of nitrogen
p_{TMA}	partial pressure of trimethylaluminum
S	surface area of silicon wafer support covered by carbon nanotubes
\bar{s}	pore wall surface area to pore volume ratio
s_0	surface area of a reactive surface site
t	time
\bar{t}	time, dimensionless
T	absolute temperature
v	mean absolute velocity from Maxwell-Boltzmann distribution
w_{II}	width of the reaction front
z	spatial coordinate of depth into the porous structure
\bar{z}	spatial coordinate of depth into the porous structure, dimensionless
z_c	depth reached by ALD coating in a given cycle in diffusion-limited regime
Greek:	
α	ratio of pore wall surface area to the total volume of membrane
β_0	initial reaction probability upon collision of precursor molecule with an available surface site (initial sticking probability)
ε	porosity
λ_b	mean free path of a precursor molecule in bulk gas
λ_f	mean flight path of a molecule confined by the porous structure
$\mu_{Al_2O_3}$	molar mass of alumina
μ_{N_2}	molar mass of nitrogen
μ_{TMA}	molar mass of trimethylaluminum
$\rho_{Al_2O_3}$	density of ALD-deposited alumina
Φ_{wall}	gas exposure experienced by walls of the porous structure
σ	fiber length per volume
τ_c	mean diffusion time until chemisorption (time unit)
τ_f	mean flight time of a molecule confined by the porous structure
θ	ALD surface coverage

Introduction

Atomic Layer Deposition (ALD) is a thin-film synthesis technique, which allows to achieve an atomic thickness precision, conformal, pinhole-free coating of highly complex substrate geometries, such as high aspect-ratio structures^{1,2}, porous structures^{3,4} and high-surface-area materials⁵. In particular, coating of carbon nanotubes (CNTs) with ALD has been a widely pursued topic, due to the attractive physical properties of CNTs, including their outstanding electrical conductivity and high surface area. ALD coating of CNTs finds applications in synthesis and tailoring the properties of novel functional materials for energy storage^{6–8}, energy conversion⁹, photocatalysis^{10–12}, biosensing^{13,14} and more.

ALD is a variant of chemical vapor deposition, which relies on a sequential exposure of the substrates to the chemical vapors, referred to as *precursors*, which undergo self-limited chemical reactions on the substrate surface, referred to as *chemisorption*. Typically, the ALD process is designed with the aim of obtaining a conformal coating. For this purpose, two main conditions need to be fulfilled. First, the substrate surface needs to have a high density of reactive surface sites, while low densities tend to result in an island-like growth instead of a conformal film^{15,16}. This issue is especially important in coating of CNTs, due to their intrinsic chemical inertness¹⁷. It has been addressed, for instance, by applying a plasma treatment^{15,16}, exposure to ozone¹⁸, a non-covalently adsorbed nucleation layer of NO₂¹⁹ or by tailoring the synthesis temperature throughout the process^{15,20}. The other condition for the conformal coating is a sufficient exposure to the precursor species^{6,19}, so that all the surface reactive sites are uniformly covered in each cycle. This necessitates both providing a sufficient amount of the precursor (relevant for the ultrahigh surface area materials), as well as letting the precursor exposure time long enough for the diffusion to drive the precursor molecules to the available reactive sites (relevant for tightly porous substrates). The diffusion and precursor supply limitation can also be turned into an advantage in synthesis of intentionally non-conformal coatings, such as fine-tuned pore openings²¹ or functional coating of the topmost features of the high aspect-ratio structure²². It becomes clear that for the design and optimization of ALD films in porous media, rigorous modelling is desirable, accounting for the gas transport and reaction kinetics, to derive corresponding universal scaling laws.

A thorough review of various approaches to the modelling of ALD on porous nanostructures can be found in the recent work of Cremers *et al.*²³, including ballistic, Monte-Carlo, continuum, analytical and semi-analytical models. In this work, we aim to describe the process behavior of ALD by a continuum model, analytically distinguish the diffusion-limited and reaction-limited ALD process, establish analytical scaling laws for coating depth in the diffusion-limited regime and surface coverage in the reaction-limited regime. The continuum model introduced in this work follows the notation of Yanguas-Gil and Elam^{24,25}. The model accounts for Langmuirian chemisorption and diffusion of the precursor species within the porous nanostructure. We derive a novel parametrization of the model in the natural system of units

imposed by the phenomena governing the process. This approach allows for elucidating the physical effect of the process parameters on the system behavior and for establishing the new scaling laws for a general case of ALD on arbitrary porous substrates. We present a new physical insight into the problem of uniform ALD coating of porous substrates, quantitatively describing the distinction of the ALD coating regimes, the single-cycle coating profile shape and their inherent interdependence. Finally, we particularize the model for the case of ALD coating of random fibrous structures and experimentally validate its performance in predicting the coating profile in a multicycle ALD coating compared to the experiment on a CNT forest substrate. Moreover, the experimental results constitute a validation of the Knudsen diffusion model in fibrous structures, developed in our previous work²⁶.

Continuum diffusion-reaction model

In the formulation of the continuum model of ALD on porous nanostructures we follow the notation of Yanguas-Gil²⁵. We parametrized the model of Yanguas-Gil to enable a straightforward determination of the physical parameters that govern the spatial and temporal behavior of the ALD coating of porous substrates. Owing to our general formulation, the model encompasses the entire variety of porous substrates, provided that the specified parameters for the given substrate structure and ALD process are determined. The model assumes a uniform diffusivity and pore surface area to pore volume ratio within the substrate, and an irreversible Langmuirian adsorption of molecules, referred to as *chemisorption*. In one dimension, the model is expressed with the following set of differential equations:

$$\begin{cases} \frac{\partial n}{\partial t} = -J_{\text{wall}}\beta_0\bar{s}(1-\theta) + D\frac{\partial^2 n}{\partial z^2}, \\ \frac{\partial \theta}{\partial t} = J_{\text{wall}}\beta_0s_0(1-\theta) \end{cases} \quad (1)$$

where n , t , D , z , β_0 , \bar{s} , J_{wall} , θ and s_0 represent volumetric gas concentration (number of gas molecules per volume), time, diffusivity, axial coordinate, reaction probability upon collision of a precursor molecule with an available surface site, pore wall surface area to pore volume ratio, gas impinging rate onto pore walls, surface coverage and an average surface area of an adsorption site, respectively.

From the classical kinetic theory of gases, the gas impingement rate is

$$J = \frac{nv}{4}, \quad (2)$$

v being the mean thermal velocity of precursor molecules. Here, however, we express the impinging rate in a more general form, specific to porous nanostructures J_{wall} :

$$J_{\text{wall}} = \frac{n}{\tau_f\bar{s}}, \quad (3)$$

where τ_f is the mean time of flight of a precursor molecule in the space confined by the nanostructure, which is related to the mean flight path length between subsequent molecule-wall collisions λ_f ,

$$\tau_f = \frac{\lambda_f}{v}. \quad (4)$$

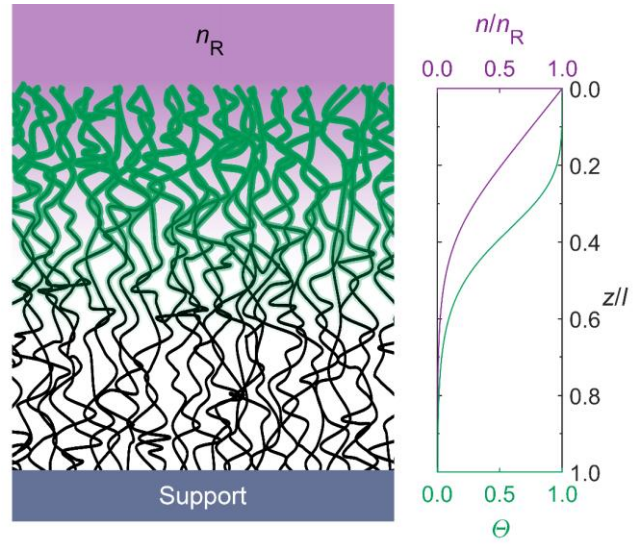


Figure 1. The main variables of the model system (1) illustrated together with a graph of its typical numerical solution. In the graph, the gas concentration in the membrane n is normalized to the gas concentration surrounding the sample n_R , whereas the depth coordinate z - to the membrane thickness l . The single-cycle ALD coverage θ is dimensionless. Color-coding: n - purple, θ - green.

Although in the cylindrical pores, the impinging rate J_{wall} as described with equation (3) is equivalent to (2), we argue that it is not the case in general, as presented in our previous work for the case of fibrous membranes²⁶. Moreover, D and \bar{s} can be set as position-dependent in 3 dimensions, reflecting the inhomogeneous geometry. In the inhomogeneous formulation of the problem, the diffusion term in the model (1) needs to be generalized as either $\partial/\partial z(D\partial n/\partial z)$ or $\nabla(D\nabla n)$, depending whether the problem is one- or three-dimensional, respectively. The anisotropy of diffusivity can be captured by expressing D as a diffusion tensor instead of a scalar, also possibly position-dependent. In this work, however we analyze the simple case of one-dimensional, position-invariable diffusion, therefore D is set as a scalar. The value or expression for D depends on the gas pressure as well²⁶, because pressure affects the mean free path of molecule in a gas and thus, determines the diffusion regime. The ratio of the mean free path in bulk gas λ_b to the mean flight length between subsequent molecule-wall collisions λ_f is referred to as *Knudsen number*, Kn ,

$$\text{Kn} = \frac{\lambda_b}{\lambda_f}. \quad (5)$$

For tightly porous structures at low gas pressures, Kn is much greater than 1, which determines the Knudsen regime of gas diffusion. In this regime, the intermolecular collisions can be neglected and the molecule flight paths are ballistic^{27,28}. In the opposite case, when $\text{Kn} \ll 1$, the diffusion occurs in a viscous regime, whereas the intermediate values of $\text{Kn} \sim 1$ define a transition regime of diffusion. The model discussed here remains valid in any diffusion regime, however when we particularize the model for the case of coating of CNT arrays, a purely Knudsen regime of diffusion is assumed. Notably, \bar{s} can be expressed as

$$\bar{s} = \frac{\alpha}{\epsilon}, \quad (6)$$

where α and ε represent the surface area to volume ratio and porosity, respectively. We are considering nanostructures fixed on planar substrates on the bottom, with the top side exposed to the precursor gas. Hence, the boundary conditions for the gas phase are

$$n(z = 0, t) = n_R(t), \quad (7)$$

$$D \frac{\partial n}{\partial z}(z = l, t) = 0, \quad (8)$$

where n_R is the precursor concentration in the reactor, to which the structure is exposed, whereas l is the total thickness of the structure. The condition (7) reflects the continuum requirement, which is that the concentration of gas at the top of the nanostructure must be the same as directly above the nanostructure, whereas the condition (8) is equivalent to forcing the gas flux to be equal zero at the coordinate of the substrateⁱ.

As we assume no precursor gas in the pores of the structure initially, the initial condition for n is

$$n(z, t = 0) = 0. \quad (9)$$

The chemisorption coverage θ , not having the flux term in its governing equation, does not require boundary conditionsⁱⁱ. As an initial condition for θ we set

$$\theta(z, t = 0) = 0, \quad (10)$$

while at the beginning of the cycle, we are expecting no coverage. The main variables of the model system (1) are illustrated in Figure 1.

Dimensionless form of the model

In the work of Yanguas-Gil²⁵, the model was reduced to a dimensionless form, taking the membrane thickness and gas concentration upon pulsing as a base for the system of units. Here however, a different reduction is presented, where the system of units is dictated strictly by the physical phenomena governing the system behavior, which leads to a dimensionless form of the equation system itself. A single solution of the dimensionless model constitutes an entire class of real physical solutions, while the solution domain scales with the units of respective quantities. This approach allows for a straightforward identification and quantification of the scaling laws that govern the behavior of the system captured by the model.

The time unit τ_c is determined by both the time of flight and the reaction probability,

$$\tau_c = \frac{\tau_f}{\beta_0}. \quad (11)$$

ⁱ Notably, if the porous membrane considered is planar and exposed from both sides, the same set of boundary conditions can be applied - in such a case, l refers to the z coordinate in the middle of the membrane thickness and the solution is given for one exposed side, the other one being symmetrical. The zero-flux boundary condition in the middle arises then from the symmetry of the problem.

It can be interpreted as a mean time until a precursor molecule is chemisorbed when the coverage θ equals 0. Consequently, the distance unit λ_c is determined by the diffusivity and the time unit,

$$\lambda_c = \sqrt{2D\tau_c}, \quad (12)$$

which represents the diffusion length of a molecule (root mean square displacement along the z axis direction due to diffusion) until chemisorption takes place at zero coverage, $\theta=0$. The unit of gas concentration is set as

$$n_0 = \frac{\bar{s}}{s_0}, \quad (13)$$

being the precursor concentration in the porous structure, for which the number of gas molecules contained in the pores equals the number of adsorption sites, i.e. the amount of gas, that would fully saturate the self-limiting chemisorption on the structure surface.

The coverage θ is naturally dimensionless and, as such, it requires no unit. It is also convenient to express the gas impingement rate J_{wall} in the dimensionless terms,

$$J_{\text{wall}} = \frac{1}{\tau_c \beta_0 s_0} \bar{n}. \quad (14)$$

Setting $(\tau_c \beta_0 s_0)^{-1}$ as the unit of J_{wall} , we obtain the dimensionless gas impingement rate equivalent to the dimensionless gas concentration. Analogously, the gas exposure onto nanostructure walls Φ_{wall} becomes

$$\Phi_{\text{wall}}(t) = \int_0^t J_{\text{wall}} dt = \frac{1}{s_0 \beta_0} \int_0^{\bar{t}} \bar{n} d\bar{t}. \quad (15)$$

Consequently, $(s_0 \beta_0)^{-1}$ is set as the natural unit of gas exposure, the physical meaning of which depends on the ALD regime, as discussed in the further part of this work. We define the gas exposure Φ onto macroscopic surfaces analogously as a time integral of the classical gas impingement rate J , expressed with equation (2).

Applying the system of units (11-13) and expressing J_{wall} in terms of the dimensionless gas concentration (14), we obtain the dimensionless form of the model (1) with no parameters:

$$\begin{cases} \frac{\partial \bar{n}}{\partial \bar{t}} = -\bar{n}(1 - \theta) + \frac{1}{2} \frac{\partial^2 \bar{n}}{\partial \bar{z}^2} \\ \frac{\partial \theta}{\partial \bar{t}} = +\bar{n}(1 - \theta) \end{cases}. \quad (16)$$

The dimensionless boundary- and initial conditions become

$$\bar{n}(\bar{z} = 0, \bar{t}) = \bar{n}_R(\bar{t}), \quad (17)$$

ⁱⁱ Some solvers might require providing the boundary conditions for θ for running properly in conjunction with the other equation containing the flux term. In such a case, one may accurately set both boundary conditions to zero flux of θ at both boundaries, analogously to (8).

$$\frac{\partial \bar{n}}{\partial \bar{z}}(\bar{z} = \bar{l}, \bar{t}) = 0, \quad (18)$$

$$\bar{n}(\bar{x}, \bar{t} = 0) = 0, \quad (19)$$

$$\theta(\bar{x}, \bar{t} = 0) = 0. \quad (20)$$

Notably, we find a direct relation of the dimensionless gas concentration \bar{n}_R to the Knudsen number, which is discussed in the further part of this work, exemplified for the specific case of randomly-oriented fibers.

ALD coating regimes and their corresponding scaling laws

The kinetics of ALD on porous nanostructures is defined by the balance between the rates of the two competing mechanisms – gas-phase diffusion and chemisorption. Depending on which one constitutes the kinetically-limiting factor to the process, the ALD occurs in a *reaction-limited regime*, a *diffusion-limited regime*^{2,25}, or between the two mentioned extremes, in what we refer to as a *transition regime*, in which the reaction rate is closely in line with the diffusion rate. The characteristic behavior of coating in the three distinguished ALD regimes is schematically illustrated in Figure 2, taking an array of vertically aligned nanotubes as an example nanoporous structure. In the reaction limited regime, the reaction probability is relatively low, which leads to multiple collisions of the precursor molecules with the walls that do not lead to chemisorption. Effectively, molecules are able to diffuse through the entire structure and react randomly anywhere on substrate surface, resulting in a uniform coating. In the diffusion-limited regime, on the other hand, the molecules diffuse freely through the already-coated topmost section of the porous structure and react at a high probability on the surface once an available surface site is encountered. It results in what is referred to as a step coverage – a front of a conformal film coating, propagating into the structure gradually with the continuing precursor exposure. The transition regime lies in between of the two mentioned extremes. For both the extreme regimes, analytical solutions of the model (1) and the resultant scaling laws are presented in the further part of this work. The transition regime requires solving (1) numerically.

The main question remains, what process parameters dictate the ALD regime and the coating profile. It has been qualitatively identified in literature, that a low reactive sticking probability β_0 results in the reaction-limited process, whereas a high Knudsen number results in a diffusion-limited ALD². Many studies have indicated, that lowering the β_0 results in a smoothening of the step-coverage profile dictated by the diffusion-limited regime^{2,29,30}. We will encompass the quantitative description of both the growth regime and the coverage profile shape with one decisive parameter – the mean diffusion path until chemisorption λ_c .

In the work of Yanguas-Gil²⁵, the Thiele number h_T was defined (sometimes referred to as Thiele modulus), which relates the ratio of the reaction rate to the diffusion rate³¹, allowing to determine the ALD regime. The criterion $h_T \gg 1$ defines a diffusion-limited regime, whereas $h_T \ll 1$ –

a reaction-limited regime. Expressing h_T in terms of the units defined in the present work,

$$h_T := l \sqrt{\frac{\bar{s}_l \text{wall} \beta_0}{nD}} = \frac{l}{\sqrt{D\tau_c}} = \frac{\sqrt{2}l}{\lambda_c}, \quad (21)$$

we find, that h_T is of the order of magnitude of the ratio of the structure thickness l and the mean diffusion path until chemisorption λ_c . Therefore, the value of λ_c compared to the thickness l determines the growth regime. It is also consistent with the dependency of the ALD regime on β_0 , while λ_c depends on β_0 as well (see equation 12). Moreover, we find that λ_c quantitatively corresponds to the width of the spread of the coating profile of a single ALD cycle, as discussed in detail further in this section, which ultimately unifies the description of the ALD regime and the coating profile shape.

Reaction-limited regime

If the molecule diffuses all the way through the structure, bouncing between the structure walls multiple times and still has a low probability that it has chemisorbed along the way, the ALD occurs in the so-called *reaction-limited regime*. This is described by the Thiele number h_T much lower than 1, or the criterion

$$\lambda_c \gg l. \quad (22)$$

In this case, before a significant coverage is reached, the gas concentration n equilibrates throughout the structure, in equilibrium with the gas concentration in the reactor n_R . The chemisorption occurs gradually, uniformly over the whole surface area of the nanostructure. To apply this extreme in the model system (1), we set $n \equiv n_R(t)$ throughout the structure, which gives a reduction of the model system to one differential equation

$$\frac{d\theta}{dt} = \frac{s_0 n_R}{\bar{s} \tau_c} (1 - \theta) \quad (23)$$

with the initial condition

$$\theta(t = 0) = 0. \quad (24)$$

The solution of this system is

$$\theta(t) = 1 - \exp\left(-\frac{s_0}{\bar{s} \tau_c} \int_0^t n_R(t') dt'\right) = 1 - e^{-\int_0^{\bar{t}} \bar{n}_R(\bar{t}') d\bar{t}'}. \quad (25)$$

Using the definition of the gas exposure Φ_{wall} (15), we obtain the coverage

$$\theta(\Phi_{\text{wall}}) = 1 - \exp(-s_0 \beta_0 \Phi_{\text{wall}}) = 1 - e^{-\bar{\Phi}_{\text{wall}}}. \quad (26)$$

Equations (25,26) constitute a scaling law for ALD coverage in the reaction-limited regime. Moreover, equation (26) reveals that in the context of the reaction-limited regime, the unit of exposure $(s_0 \beta_0)^{-1}$ can be understood as the characteristic exposure that provides surface coverage fraction equal to $1 - e^{-1}$. If the n_R can be assumed constant over the timespan of the precursor exposure, we obtain θ conveniently expressed in terms of dimensionless quantities,

$$\theta(t) = 1 - \exp\left(-\frac{s_0 n_R}{\bar{s} \tau_c} t\right) = 1 - e^{-\bar{n}_R \bar{t}}. \quad (27)$$

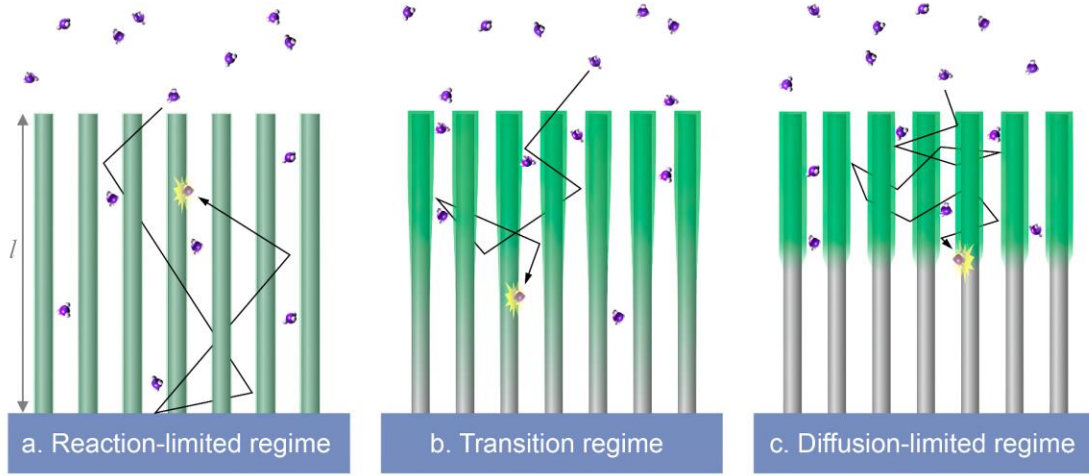


Figure 2. Illustration of the three distinct coating regimes of porous nanostructures, exemplified by vertically aligned cylinder array as a substrate; a) reaction-limited regime, b) transition regime, c) diffusion-limited regime. Green color represents the chemisorption coverage. The thickness of the porous substrate is denoted with l .

Transition regime

In the transition regime, the diffusion and reaction rate are of the same order of magnitude. In this case, a significant fraction of the precursor molecules manages to diffuse all the way through the structure and not chemisorb. Still, however, a considerable fraction of the precursor molecules get chemisorbed on the way. For this case, the regime condition is

$$\lambda_c \sim l, \quad (28)$$

or the Thiele number of the order of unity. Simple analytical approximate solutions of the model system (1) are not available for this regime. The solution needs to be evaluated numerically.

Diffusion-limited regime

If the molecule is only able to travel a short path within the porous structure until it chemisorbs, relative to the whole depth of the structure to coat, the diffusion is the limiting factor in the process. Hence, the diffusion-limited ALD process is defined by Thiele number h_T much greater than 1, or by the condition

$$\lambda_c \ll l. \quad (29)$$

The following derivation is based on the considerations of Gordon *et al.*³², which focused on ALD in narrow holes and trenches. Here, however, we are expressing the coating kinetics for the case of a general nanoporous material, at the same time pinpointing the geometrical and physical parameters that are determining the coating behavior.

Solving the equation system (1) for two selected diffusion-limited regime conditions, namely $l=100 \lambda_c$ and $l=1000 \lambda_c$, $n_R=0.01 \bar{s}/s_0$ in both cases, we obtain solutions for the gas concentration and chemisorption as shown in Figure 3.

In the solution one can distinguish three characteristic zones: I – complete coverage zone, II – reaction front and III – no-coverage zone. In the zone I, the coverage is saturated, $\theta = 1$, whereas the concentration exhibits a uniform gradient in this zone, bound by the left-sided condition $n(x=0) = n_R$. The zone II follows deeper, where the

coverage is not yet complete, $0 < \theta < 1$, whereas the concentration n approaches zero, because the rapid chemisorption of molecules acts as a vacuum pump. The width of this zone is proportional to the length unit λ_c . In Figure 3, the reaction front is marked with a grey overlay of width equal to $4 \lambda_c$.

In the zone III, the $\theta = 0$ and $n = 0$, while the precursor had no chance to reach it, getting consumed by chemisorption along the way within the reaction front.

It is evident that in the diffusion-limited regime, we observe that the coating proceeding into the structure can be approximated with a step-function, where zone II determines the location of the step. The scaling law of coating depth in this regime is proposed as

$$z_c(\Phi_{\text{wall}}) = \sqrt{2D\tau_f s_0 \Phi_{\text{wall}}} = \lambda_c \sqrt{s_0 \beta_0 \Phi_{\text{wall}}}, \quad (30)$$

where z_c is the coating depth and Φ_{wall} is the gas exposure experienced by the topmost walls of the porous structure (close to $z = 0$). The derivation of (30) can be found in Appendix A (Supporting Information). Scaling law (30) can be applied to any nanoporous structure, provided that its parameters are determined. In the context of diffusion-limited ALD regime, the exposure unit $(s_0 \beta_0)^{-1}$ represents an exposure, for which the porous nanostructure is coated down to the depth λ_c . If the gas concentration is constant throughout the pulse and equal n_R , the scaling law (30) becomes

$$z_c(t) = \lambda_c \cdot \sqrt{\frac{n_R s_0}{\bar{s}} \frac{t}{\tau_c}}. \quad (31)$$

Taking into account, that λ_c is a measure of the mean path that molecule travels in the random walk until chemisorption, we take an educated guess, that it directly reflects the characteristic width of the reaction front w_{II} . Namely we state that

$$w_{II} = \lambda_c. \quad (32)$$

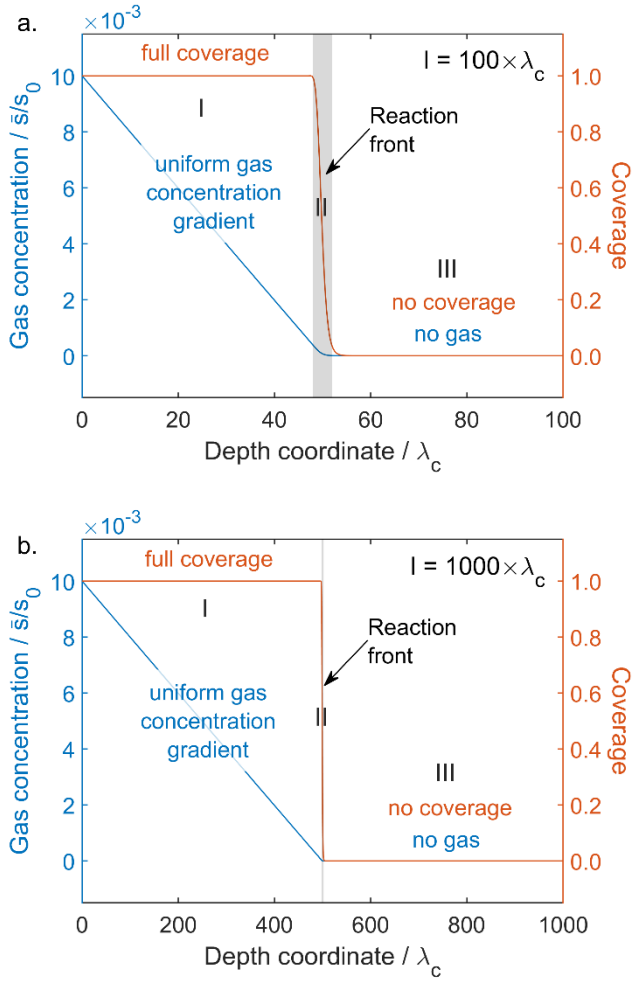


Figure 3. Two example solutions of the model (1) for the diffusion-limited regime: a) $l = 100 \lambda_c$, b) $l = 1000 \lambda_c$, for both $n_R = 0.01 \bar{s}/s_0$. Gas concentration and coverage curves are plotted with respect to the depth coordinate. Three distinct zones are indicated with roman numerals: I - complete coverage zone; II - reaction front and III - no-coverage zone.

The validity of (32) depends on the definition of w_{II} . Let us assume, that the blurred coverage step function, like the ones shown in Figure 3, can be described as a convolution of a Heaviside step function H and a smoothing filter function, f . Effectively, it means that the ideal sharp step-like coverage undergoes low-pass filtering. Let us define w_{II} as the square root of the variance of f . We perform a deconvolution and extract the z_c and w_{II} from the numerical solutions of the system (1) obtained for parameters fulfilling the condition of molecular gas transport regime ($Kn \gg 1$) and diffusion-limited regime of ALD (29). The exact procedure is described in Appendix B (Supporting Information). The results shown in Figure 4 confirm a remarkable agreement of the scaling laws (31) and (32) with the numerical solutions. The slight fluctuation of the numerical values of w_{II} is attributed to numerical errors. We attribute the drop of w_{II} at the end of the coating to the edge effect, which occurs when the coating depth z_c approaches the total thickness of the system l .

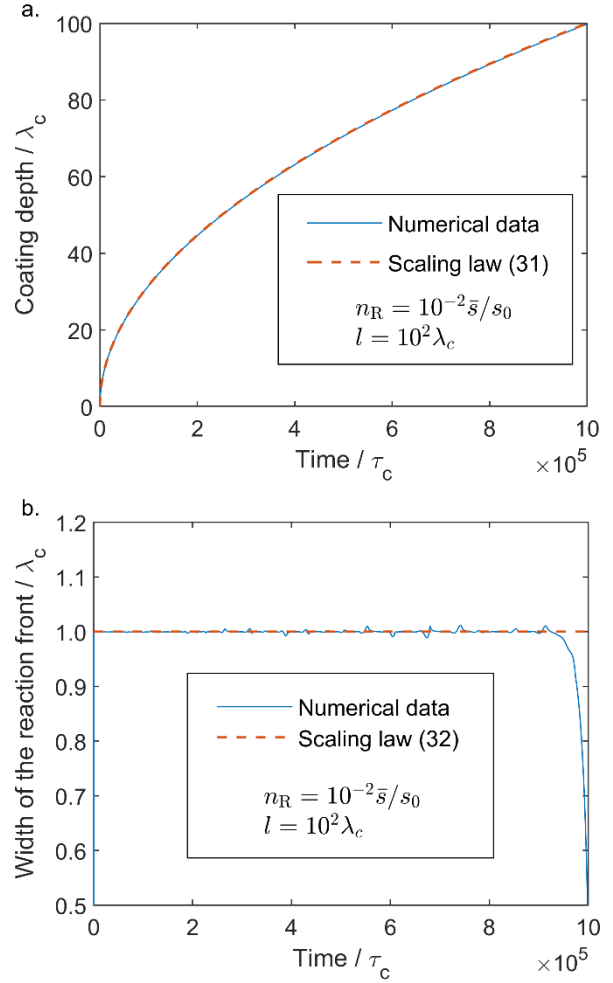


Figure 4. Numerical solutions of the system (1) compared to the respective scaling laws: a) the coating depth (31) and b) the width of the reaction front (32).

Specifying the model parameters for the case of ALD on random fibrous media

In our previous work²⁶ we derived a novel theoretical framework for the diffusion of gas in random fibrous materials. We are using a set of expressions from that work in the development of the ALD model presented here. For the truly randomly oriented fibers, which are allowed to intersect, the surface area to volume ratio α is expressed as

$$\alpha = \sigma \pi d \exp\left(-\sigma \frac{\pi d^2}{4}\right), \quad (33)$$

where d is the average fiber diameter, and σ is the fiber length per volume. The expression for porosity ε is

$$\varepsilon = \exp\left(-\sigma \frac{\pi d^2}{4}\right). \quad (34)$$

The ratio of (33) and (34) gives the surface area to pore volume ratio \bar{s} ,

$$\bar{s} = \frac{\alpha}{\varepsilon} = \sigma \pi d. \quad (35)$$

The mean flight time between the subsequent molecule-wall collisions τ_f is expressed as

$$\tau_f = \frac{\pi^2}{2} \frac{1}{\bar{s} v}, \quad (36)$$

where v is the mean absolute velocity of gas molecules from the Maxwell-Boltzmann distribution. While we are assuming that the diffusion occurs in the molecular regime, we are using the equation for Knudsen diffusivity D ,

$$D = \frac{\pi^2 v}{6 \bar{s}}. \quad (37)$$

If a pure Knudsen gas diffusion regime cannot be assumed due to high pressures, one can implement the diffusivity equation accounting for the transition to the viscous regime presented in our previous work²⁶. The Knudsen number for fibrous structures Kn is expressed as

$$\text{Kn} = \frac{\sqrt{2} \bar{s} k_B T}{\pi^3 p d_m^2}, \quad (38)$$

where k_B is the Boltzmann constant, T is the gas temperature in K, p is the peak gas pressure, whereas d_m is the diameter of a precursor gas molecule. From the classical gas kinetics,

$$\frac{p}{k_B T} = n_R. \quad (39)$$

Moreover, we can assume that d_m^2 is approximately equal to the average area of an adsorbate surface site s_0 . Hence,

$$\text{Kn} \approx \frac{\sqrt{2} \bar{s}}{\pi^3 n_R s_0} = \frac{\sqrt{2}}{\pi^3} \frac{1}{\bar{n}_R}. \quad (40)$$

From equation (40) we can see, that for random fibrous membranes, the Kn is uniquely determined solely by the dimensionless gas concentration \bar{n}_R , which further elucidates the physical relevance of the system of units defined. Clearly, for the assumption of the molecular regime of the gas transport, the \bar{n}_R needs to be much smaller than 1, so that the Kn is much greater than 1. Notably, Yanguas-Gil *et al.*^{24,25} define an *excess number*, which is analogous to \bar{n}_R . The excess number determines whether a so-called *frozen surface approximation* of the system can be assumed, i.e. whether an equilibration of the distribution of gas within the pores of the structure is much faster than the surface saturation. The relation (40) shown here elucidates that this property is intrinsically connected with the gas transport regime. This finding means that if the diffusion occurs in the Knudsen regime, utilization of the frozen surface approximation is necessarily justified.

Coating profile of random fibrous nanostructures in a diffusion-limited ALD regime

While coating porous nanostructures with ALD in a diffusion-limited regime, the coating depth gradually decreases from cycle to cycle, see Figure 5. It happens so because each cycle makes the structures tighter for the gas diffusion (decrease in ε), thus decreasing the Knudsen diffusivity. The other factor influencing the coating depth is a change in the surface area to volume ratio α from cycle to cycle. It affects both the Knudsen diffusivity and the amount of precursor required to saturate the given thickness of the porous structure as the surface area to be coated changes. Depending on the type of the structure, regular or inverse, α gradually decreases or increases, respectively, as the film grows, as discussed in our previous work²⁶.

To mitigate the diffusion-limiting effect and achieve a consistently uniform coating in each cycle, one needs to adjust the gas exposure Φ_{wall} following the scaling law (31)

according to the proceeding changes in surface area, porosity and diffusivity from one cycle to another. To examine the performance of the scaling law, we have carried out an experiment of the diffusion-limited coating in an undersaturated mode, i.e. the coating depth z_c is less than the thickness of the porous mat to coat. The scaling law (30) allows to predict the ALD coating profile, which we perform here on the example of CNT mat as a model substrate.

Given the framework of expressions introduced for the random fibrous geometry, the scaling law for the coating depth in the diffusion-limited regime (30) becomes

$$z_c(\Phi_{\text{wall}}) = \frac{\pi}{\sigma d} \sqrt{\frac{s_0}{6}} \Phi_{\text{wall}}. \quad (41)$$

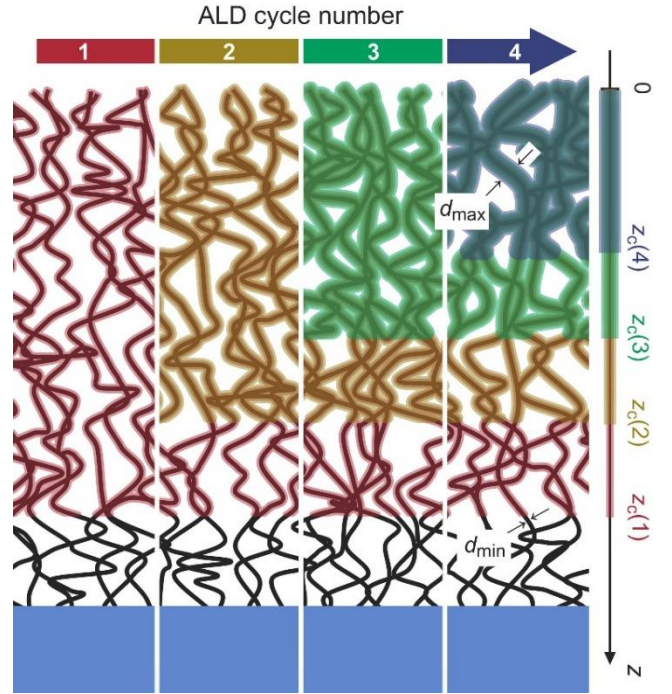


Figure 5. Schematic of ALD coating profile on a fibrous nanostructure on a flat support (not to scale) illustrating the decreasing coating depth z_c in subsequent ALD cycles; the numbers of the respective ALD cycles are given in brackets (1, 2, 3 and 4). Minimum and maximum fiber diameters are indicated as d_{\min} and d_{\max} , respectively. The effect of decreasing coating depth in subsequent cycles is largely exaggerated in this figure, for illustration purposes.

Transformation of equation (41) gives the coating profile,

$$d(z) = \begin{cases} d_{\max} & \text{for } d_{\text{aux}}(z) > d_{\max} \\ d_{\text{aux}}(z) & \text{for } d_{\min} < d_{\text{aux}}(z) < d_{\max}, \\ d_{\min} & \text{for } d_{\min} > d_{\text{aux}}(z) \end{cases} \quad (42)$$

where $d(z)$ is the CNT diameter including the coating with respect to the depth into the mat z , d_{\min} is the initial fiber diameter, d_{\max} is the diameter of the coated fiber measured at the top of the structure, where all the coating cycles are saturated. The $d_{\text{aux}}(z)$ is an auxiliary variable defined for convenience,

$$d_{\text{aux}}(z) := \frac{k}{z}, \quad k = \frac{\pi}{\sigma} \sqrt{\frac{s_0}{6}} \Phi_{\text{wall}}. \quad (43)$$

Equations (42,43) describe the diameter profile for a constant precursor exposure in each cycle for coating of fibrous substrates in a multicyle ALD process. We are using this profile in the further part of the work for interpretation of the experimentally measured diameters of the ALD-coated CNT array. The diameter profile (42,43) is schematically illustrated in Figure 6.

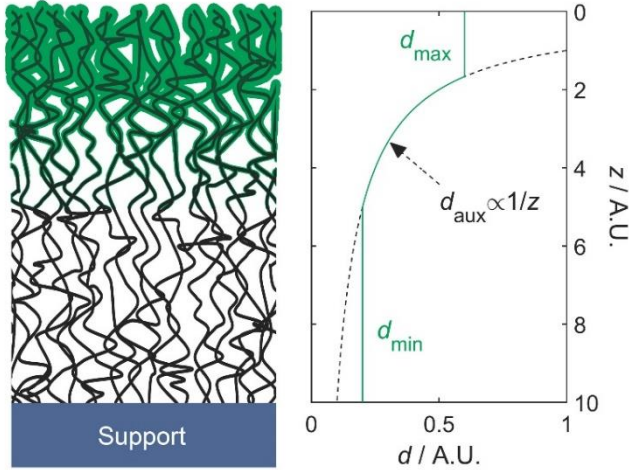


Figure 6. Schematic illustration of the diameter profile of CNTs coated with multicyle ALD in a diffusion-limited regime as described with equations (42,43); d – coated CNT diameter, z – depth coordinate, both shown in arbitrary units for illustrative purposes.

Experimental

The CNTs were synthesized on a silicon wafer by means of catalytic chemical vapor deposition, as described in more detail in our previous work³³. SEM imaging showed that the thickness of the CNT mat was ca. $300 \pm 5 \mu\text{m}$. In order to achieve and examine the diffusion-limited coating of the CNTs arrays, we performed ALD of Al_2O_3 on a CNT mat. The details of the ALD procedure are given in a following section. Subsequently, we carried out the SEM imaging of the coated CNT sample cross section in order to obtain the diameter profile data along the depth into the CNT mat. Subsequently, a theoretically expected diameter profile (42,43) and its confidence intervals are predicted based on the measured physical parameters of the model and their uncertainties. The predicted and measured coating profiles are compared to assess the performance of the model.

The parameters determining the profile are the average area of a surface site s_0 , the axes length per volume of the CNTs σ , the precursor exposure Φ_{wall} and the mean CNT diameters prior to- and after the ALD coating, d_{min} and d_{max} , respectively. The s_0 can be realistically estimated

from the growth per cycle h in terms of thickness increment in each ALD cycle³⁴,

$$s_0 = \frac{\mu_{\text{Al}_2\text{O}_3}}{2\rho_{\text{Al}_2\text{O}_3}N_A h} \quad (44)$$

where $\rho_{\text{Al}_2\text{O}_3}$ is the density of the ALD-synthesized alumina being approximately 3.0 g/cm^3 ^{35,36}, N_A – the Avogadro number, whereas $\mu_{\text{Al}_2\text{O}_3}$ – molar mass of the aluminum oxide. Division by 2 in equation (44) comes from the fact, that two TMA molecules are required to deposit one stoichiometric unit of Al_2O_3 . For internal consistency, we are deriving the h from the difference between the diameters of the CNTs before and after the multicyle ALD, d_{min} and d_{max} , respectively:

$$h = \frac{d_{\text{max}} - d_{\text{min}}}{2N_{\text{cyc}}}, \quad (45)$$

where N_{cyc} is the number of the ALD cycles. The d_{min} and d_{max} are determined by analysis of SEM images, as discussed in the further part of this work.

The absolute surface area of the coated CNTs is determined experimentally by Krypton adsorption, which allows to uniquely determine the CNT axes length per volume σ with equation (33) coupled with the given diameter profile. The procedure is explained in more detail in the further part of this work.

The exposure Φ_{wall} is determined by analyzing the pressure curve recorded during the pulsing of TMA, which is elaborated on in the following sections.

Ultimately, when all the parameters and their uncertainties are set, the validity of the gas diffusion model introduced in this work is examined – the theoretically expected coating profile is evaluated and compared to the profile directly measured by SEM.

Atomic layer deposition procedure

The ALD process has been carried out in a commercial ALD reactor Savannah 100 (Cambridge Nanotech) in a viscous flow modeⁱⁱⁱ. The temperature of the chamber was set to $225 \text{ }^\circ\text{C}$, the high-purity nitrogen (99.9999 % purity) at 20 sccm was used as a carrier gas throughout the procedure with the vacuum pump always on. As precursors for Al_2O_3 coating, we used the TMA (Sigma-Aldrich, deposition-system grade) and ozone generated by an ozone generator (OL80F by Ozone Lab[™]).

It is known that the CNTs surfaces are chemically inert¹⁷, which may result in a spot-wise nucleation of ALD films. To increase the reactivity of the intrinsically inert CNTs, we first exposed them to ozone for 33 s in a pulsed manner: 100 ms long pulses separated by 1 s, afterwards letting the reactor get purged for 40 s. An analogous approach has been successfully applied in conformal coating of graphene with alumina ALD³⁷.

ⁱⁱⁱ Within the range of pressures in our experiments, the mean free path of molecules is of the order of magnitude of micrometers ($\lambda_b \approx 20 \mu\text{m}$, see: Table 3), which is much shorter than the characteristic dimensions of the ALD reactor.

Therefore the Knudsen number in the reactor is much smaller than 1 and the viscous flow is justified.

Subsequently, in order to eliminate the influence of the differences in surface chemistry of ALD on carbon and on alumina in our experiments, we initially coated the CNTs with 5 cycles of seed layer, ensuring a saturated conformal coating by long pulsed exposures to the precursors. Single cycle description: 10×150 ms TMA pulse separated by 1 s, 40 s waiting time; 10×100 ms ozone pulse separated by 1 s, 40 s waiting time.

Ultimately, the diffusion-limited coating has been conducted on such prepared substrate. 75 coating cycles have been carried out, each cycle was done as described: 1×100 ms TMA pulse, 40 s waiting time, 10×100 ms ozone pulse separated by 1 s, 40 s waiting time. Finishing the process, the reactor was cooled down to 80 °C and sample was extracted. The ALD processing is summarized in Table 1.

Table 1. Summary of the ALD processing protocol.

Repetitions		Event	Duration
1×	30×	O ₃ pulse	100 ms
		wait	1 s
	1×	wait	40 s
5×	10×	TMA pulse	150 ms
		wait	1 s
	1×	wait	40 s
	10×	O ₃ pulse	100 ms
		wait	1 s
1×	wait	40 s	
75×	1×	TMA pulse	100 ms
		wait	40 s
	10×	O ₃ pulse	100 ms
		wait	1 s
1×	wait	40 s	

Establishing the precursor gas exposure from pressure curves

The pressure curve recorded during TMA pulsing allows to determine the exposure Φ_{wall} . In principle, for an accurate estimate, one needs to carry out a complex simulation, involving fluid dynamics, modelling of the vacuum pump, precursor evaporation, etc. We are however suggesting a simplistic approach to the issue with several assumptions:

- One can treat the function of pressure versus time in the ALD reactor upon precursor pulsing as an “impulse response” to the delivered gas, in analogy to signal processing.
- The response is approximated as a decaying exponential, which reflects the vacuum pumping behavior.
- A plug-flow of gas is assumed for simplicity.
- The flux of precursor gas during pulsing can be approximated as a temporal Gaussian peak.

The decaying exponential function is a pressure response to the infinitesimally short precursor pulse (temporal Dirac

delta). The time constant of the decaying exponential is subject to curve fitting. Effectively, while the precursor pulse is approximated as a Gaussian, the pressure curve is predicted as a response to a Gaussian-shaped precursor pulse, which is calculated as a convolution of the Gaussian and the decaying exponential. Such a curve is fit to the pressure data points, and the gas exposure experienced by the sample is extracted. The example pressure graph and the calculation results are shown in Figure 7. The data analysis process is elaborated on in Appendix C (Supporting Information). By integration of the resulting impinging rate over time, we obtain the exposure $\Phi_{\text{wall}}=(6.76\pm 0.68)\times 10^{19}$ cm⁻², where the confidence interval is 95% and comes from the analysis of 10 pulsing curves.

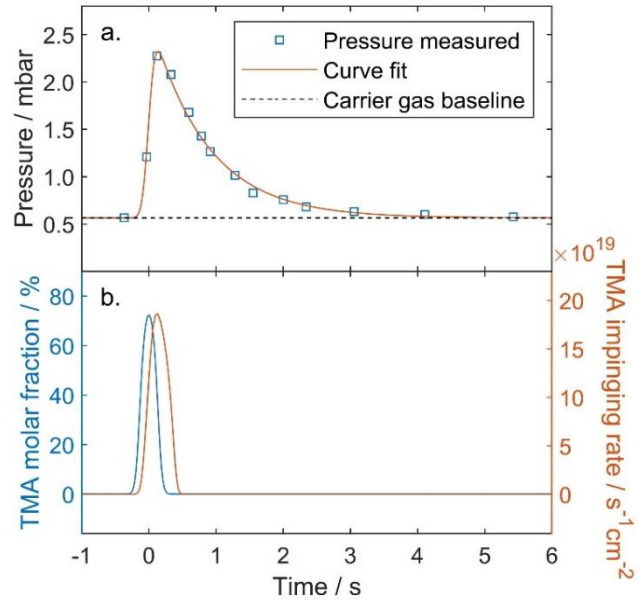


Figure 7. Evaluation of temporally-resolved impingement rate based on the analysis of the pressure recorded during TMA pulsing; a) a typical pressure curve as observed upon 100 ms TMA pulsing, with the correction for the base pressure and a model curve fit; b) TMA molar fraction at the inlet to the reactor and the impinging rate J_{wall} evaluated based on the model curve fitting result.

Scanning Electron Microscopy Imaging

In order to investigate the diameter profile of the alumina-coated CNT mat in the diffusion-limited ALD, we performed scanning electron microscopy (SEM) imaging. A fragment of CNT forest has been carefully removed with a razor, exposing the cross section of the coated mat. The imaging has been done with the Hitachi S4800 SEM at a 45° sample tilt. An overview image along with three example high-magnification images is shown in Figure 8. The imaging shows, that the top part of the CNT array is uniformly coated with the alumina giving a high contrast. Further deep into the structure, the structure appears gradually darker in the overview, which is linked to a declining coating thickness, as seen in the high-magnification images, and as expected from the coating in the diffusion-limited regime.

High-magnification images have been taken at 20 different depths into the structure. The images were analyzed in the

open-source ImageJ software; 10 diameters were measured by hand in each image for appreciable overall statistics. To avoid the human bias in the measurement, the images were first shuffled, and subsequently the measurements obtained were assigned to their respective original positions accordingly.

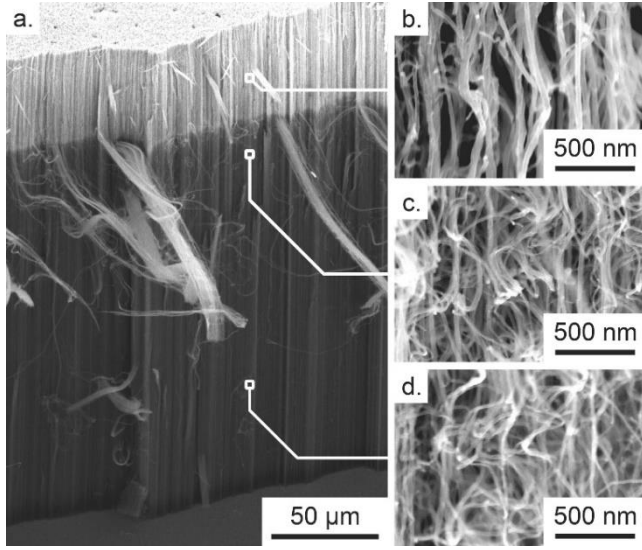


Figure 8. Scanning electron microscopy imaging of the alumina-coated CNTs; a. - overview of the CNT forest tilted by 45°; b., c., d. - high magnification images at depths of ca. 40 μm , 90 μm and 240 μm , respectively.

Measurement of surface area by Krypton adsorption-desorption isotherms

The absolute surface area of the coated CNTs was determined by the Brunauer-Emmet-Teller (BET) method. Krypton adsorption-desorption isotherms of the silicon wafer with the alumina-coated CNTs were collected at 77 K using a Micromeritics 3Flex Surface area and Porosity Analyzer. Prior to the measurement, the sample was degassed for 20 h at 200 °C at a pressure of 1.3×10^{-2} mbar in order to remove water vapor and volatile organic compounds. Data points were recorded at a relative pressure (P/P_0) range between 0.02 to 0.62 and both adsorption and desorption branches were collected. In order to get reproducible results, the sample was measured 3 times. The BET method was used to determine the absolute surface area³⁸. The resulting absolute surface area was measured as $A = 1182 \pm 63 \text{ cm}^2$, where the confidence interval is 95%, estimated as a double standard deviation. The surface area of the silicon wafer substrate is negligible compared to the total surface area measured. The value obtained by this method allows to uniquely determine the fiber axes length per volume σ , by equation (33) coupled with the diameter profile, as elaborated on in the next paragraph.

Analysis of the diffusion-limited coating profile

The diameter profile model of the multicycle ALD-coated CNTs (42,43) was found to be highly sensitive to deviations of the model parameters. Therefore, in order to obtain a reliable estimate of the expected coating profile and its confidence intervals, we implemented a *bootstrap* approach. The bootstrapping relies on random data

sampling with replacement carried out multiple times, calculating the estimators of interest in each randomization and ultimately obtaining distributions of the estimators.

The profile model (42,43) has three independent parameters: d_{\min} , d_{\max} and k . The d_{\min} was determined in each bootstrap iteration as a mean value of randomly selected diameter measurements at depths higher than 110 μm , which we found to be deep enough, so that the diffusion-limited coating depth does not reach it at any cycle. If the number of measurements performed deeper than 110 μm was N_d , then N_d random draws from the measurement pool were performed with replacement, that is, each subsequent randomly drawn measurement is returned back to the pool, which follows the most common implementation of bootstrap. Analogously, the d_{\max} was estimated in each bootstrap iteration for measurements taken at depths less than 50 μm . The parameter k requires information about the gas exposure Φ_{wall} and σ , therefore both of them need to be determined. To do so, in each bootstrap iteration, the exposure Φ_{wall} and the total surface area A are randomly drawn from their respective Gaussian distributions, taking the mean and standard deviations as the distribution parameters. By definition, A can be calculated as

$$A = S \int_0^l \alpha(x) dx = S \int_0^l \sigma \pi d(x) \exp\left(-\sigma \frac{\pi d^2(x)}{4}\right) dx, \quad (46)$$

where S is the surface area of the Si wafer substrate covered by the CNT mat. The parameter k is then obtained in each bootstrap iteration as a result of numerical solution of the system of equations (42,43,46). In the same procedure, σ is simultaneously obtained.

The number of bootstrap iterations in this work was set to 10^4 . The results are presented in Figure 9 and the set of the relevant parameters is gathered in Table 2. The confidence intervals shown in the figure were calculated based on all the statistics obtained from the bootstrap. The graph in Figure 9 shows an excellent agreement of the experimentally obtained coating profile and the theoretical prediction. The location and slope of the steep edge of the coating profile are predicted accurately, within the established confidence intervals, which constitutes validation of the modelling provided in this work. The growth per cycle h is found to be consistent with the values reported typically in literature^{39,40}.

Discussion

The modelling introduced in this work and its fit to the experimental data allowed to evaluate a range of physical parameters of the system, as well as their evolution with the growing ALD film. We summarize the parameters in this section, for a straightforward comparison of the system of Al_2O_3 ALD on CNT mats in our experimental configuration to other related systems. Notably, under conditions of our experiments (temperature 225 °C and peak pressure of less than 2.5 mbar), TMA vapor exists mostly in monomeric form^{41,42}. Therefore, for simplicity, we consider only TMA monomers in the following calculations. To account for the dimers (which prevail in gas phase below 75°C), one would need to scale relevant parameters appropriately, as we present in Appendix D (Supporting Information).

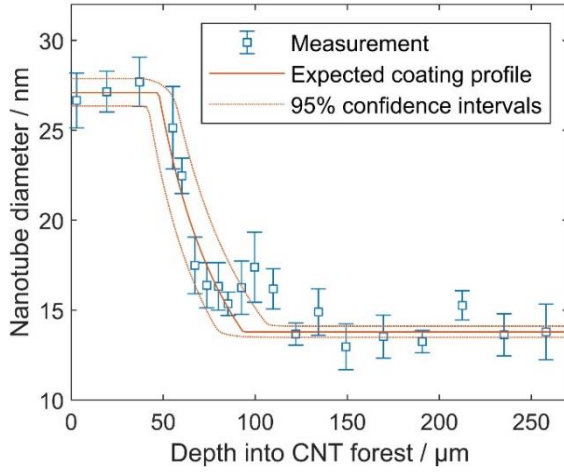


Figure 9. Measured diameters of the coated CNTs at a constant precursor exposure at each cycle together with the expected coating profile evaluated based on the measured parameters and the model presented in this work. The dotted lines indicate the 95% confidence interval of the expected coating profile resulting from uncertainties of the individual parameters determining the profile.

Table 2. The relevant parameters of the system and their confidence intervals resulting from measurements (a) and inferred from the bootstrap calculations (b).

Parameter	Value±Uncertainty	Unit
d_{\min}^a	13.79±0.31	nm
d_{\max}^a	27.10±0.76	nm
h^a	0.888±0.055	Å
Φ_{wall}^a	(6.76±0.68)×10 ¹⁹	cm ⁻²
σ^b	(4.63±0.65)×10 ¹⁰	cm ⁻²

The evaluation of Knudsen number Kn requires additional discussion. While only the high values of Kn characterize the Knudsen diffusion regime, we made sure to not overestimate its value, to have the highest confidence, that the system is indeed governed by Knudsen diffusion. It means obtaining a realistically low estimate for the mean free path in the bulk gas. Equations for Kn (38-40) were introduced for a simplified case of only the precursor gas present. Neglecting the carrier gas might, however, lead to an overestimation of the mean free path λ_b and Kn, which, as mentioned above, is to be avoided. Therefore, the estimation about to be shown here accounts for the influence of the carrier gas (here: nitrogen) on the mean free path of TMA in the bulk gas λ_b and, consequently, Kn, following the definition (5). According to the classical molecular kinetic theory⁴³, the mean free path of a molecule in a binary mixture is expressed as

$$\lambda_b = \frac{k_B T}{\pi \sqrt{2} d_x^2 p_{\text{TMA}} + \pi \sqrt{1 + \frac{\mu_{\text{TMA}}}{\mu_{\text{N}_2}} \left(\frac{d_{\text{TMA}} + d_{\text{N}_2}}{2} \right)^2} p_{\text{N}_2}} \quad (47)$$

where d_x is a kinetic diameter of a molecule, p_x – partial pressure, μ_x – molar mass. The subscripts x denote the gas mixture component. The kinetic diameter of nitrogen is established as 3.64 Å⁴⁴. We estimate the kinetic diameter of

TMA based on the average surface area of a reactive surface site s_0 assuming a close-packed arrangement of spherical molecules,

$$d_{\text{TMA}}^2 = \frac{2}{\sqrt{3}} s_0, \quad (48)$$

which gives the value of $d_{\text{TMA}} = 6.06 \pm 0.19$ Å, consistent with literature⁴⁵.

The partial pressures of TMA and nitrogen over the sample with respect to time are evaluated for a typical precursor pulse curve, as described in Appendix C (Supporting Information). The particular point in time is selected, for which the combination of partial pressures gives the smallest estimate of λ_b , which falls at the maximum of the partial pressure of TMA over the sample.

The experiment carried out in this work does not allow to fit or evaluate the reactive sticking probability β_0 , but it enables us to estimate its lower limit. While in the experiment, the ALD coating was done in the diffusion-limited regime within the entire range of the diameter of the coated CNTs, we obtain a lower estimate of β_0 for the initial diameter d_{\min} . From the condition (22) we obtain

$$\beta_0 \gg \frac{2D\tau_f}{l^2}, \quad (49)$$

which results in the requirement for β_0 to be much greater than 5.7×10^{-7} . It means, that β_0 has to be at least an order of magnitude greater than this value, so that the ALD occurs in a diffusion-limited regime, as it did in the experiments presented. This is however a very conservative estimate. Precise investigation of sticking probability of ALD precursors, TMA particularly, is a topic currently widely pursued in the ALD community. So far, it has been best studied for the classical ALD of alumina with TMA as an aluminum precursor and water as an oxidizer (TMA+H₂O ALD). The recent work of Vandalon *et al.*⁴⁶ provided a precise measurement of sticking coefficient of TMA in TMA+H₂O ALD, obtaining a value of $\beta_0 = (3.9 \pm 0.4) \times 10^{-3}$, consistent also with other studies, such as another recent work of Gakis *et al.*⁴⁷. In our process, we used ozone as an oxidizer (TMA+O₃ ALD), therefore the surface termination prior to TMA exposure is of a different chemical character than in the TMA+H₂O ALD. However, it is safe to assume that the sticking probability is in this case of the same order of magnitude. Therefore, in the further evaluations of the parameters dependent on β_0 , we are using the value found by Vandalon *et al.*

The mean absolute velocity of TMA from Maxwell-Boltzmann distribution is given with

$$v = \sqrt{\frac{8N_A k_B T}{\pi \mu_{\text{TMA}}}}, \quad (50)$$

where N_A is the Avogadro's constant. Equation (50) gives the value of $v = 392$ m/s. The expected values and uncertainties of the parameters are evaluated by the following procedure. We generated 10⁴ normally distributed instances of each of the quantities from Table 2, of β_0 obtained by Vandalon *et al.* and of CNT mat thickness $l = 300 \pm 5$ μm. Subsequently, the value for each instance was evaluated based on an appropriate equation introduced in this work. Ultimately, the value and uncertainty of each parameter were calculated as average and 95% confidence

range of the resultant, respectively. If a given parameter is affected by the CNT diameter, we show the values for both d_{\min} and d_{\max} , to elucidate how its value evolved with the proceeding ALD process. The gas impingement rate J_{wall} is estimated at the maximum TMA concentration. The evaluated parameters are gathered in Table 3. Dashes in the "Unit" column of the table reflect that the given quantity is dimensionless. If the given parameter is affected by the value of CNT diameter, Table 3 lists two values of the parameter, corresponding to d_{\max} and d_{\min} in the first and second row, respectively. All values are shown up to 2 significant digits of their respective uncertainty. Parameters denoted with a superscript V were determined assuming the sticking probability of TMA based on the results of Vandalon *et al.*⁴⁶.

Summary and conclusions

In the present work, we revisited continuum modelling of ALD on porous substrates. A new parametrization of the model system has been introduced, based on the natural scales of the physical phenomena that govern the process, which are gas diffusion and chemisorption. The model expressed in its natural system of units returns entire classes of scalable solutions, which offer ease in determining the relevant scaling laws governing the described processes. This approach revealed a clear, direct and quantitative connection between the single-cycle ALD coating profile and the determination of the ALD regime (diffusion- or reaction limited). Moreover, we have shown, that the gas diffusion regime (determined by Knudsen number) and so-called excess number (ratio between gas equilibration rate and surface reaction rate) are two sides of the same coin, being determined by the same physical parameters and, as such, they are directly coupled to one another, as per equation (40).

We presented a way to estimate the mean diffusion path until chemisorption with equation (12), which, compared to the thickness of the porous structure to coat, allows to simultaneously determine the ALD regime and the width of the reaction front for step coverage. Scaling laws given with equations (25) and (26) give an estimation of ALD coverage in the reaction-limited regime at given precursor exposure, which is useful for optimizing the precursor usage for an effective ALD coating. Scaling laws in equations (30) and (31) enable estimation of the depth into the structure coated by ALD in a diffusion-limited regime and can be used to optimize the precursor usage for conformal coating or to tailor the process to coat down to a specific depth into the porous substrate.

We particularized the model for the case of diffusion-limited multicycle ALD coating of CNT forests, applying the theoretical framework of gas transport in random fibrous media. We found a remarkable agreement between the theoretically predicted coating profile based on the determined process parameters and the directly measured coating profile with SEM imaging. The findings in this work constitute a significant contribution to the understanding of ALD on porous structures in general and on random fibrous mats in particular.

ASSOCIATED CONTENT

Supporting Information. PDF document containing Appendices A-D mentioned in the main text with detailed derivations. This material is available free of charge via the Internet at <http://pubs.acs.org>.

AUTHOR INFORMATION

Corresponding Author

* Wojciech.Szmyt@empa.ch

Present Addresses

^o Laboratory for Advanced Materials Processing, Empa, Swiss Federal Laboratories for Materials Science and Technology, Feuerwerkerstrasse 39, CH-3602 Thun, Switzerland

Author Contributions

Szmyt Wojciech: Conceptualization, Methodology, Software, Formal analysis, Investigation, Writing - Original Draft, Visualization. Guerra-Nuñez Carlos: Conceptualization, Writing - Review & Editing. Lukas Huber: Investigations, Writing - Original Draft. Dransfeld Clemens: Writing - Review & Editing, Supervision, Project Administration, Funding Acquisition. Utke Ivo: Conceptualization, Writing - Review & Editing, Supervision, Project Administration.

Funding Sources

The work presented here has been financially supported by the Swiss Nanoscience Institute (SNI PhD project P1402).

ACKNOWLEDGMENT

The authors cordially thank the members of the Nanolino group at the Physics Department, University of Basel, Switzerland and members of the Swiss Nanoscience Institute for insightful comments and suggestions. Moreover, the authors also acknowledge Michel Calame (Transport at Nanoscale Interfaces Laboratory, Empa, Dübendorf, Switzerland) for providing access to infrastructure.

ABBREVIATIONS

ALD atomic layer deposition, CNT carbon nanotube, SEM scanning electron microscope, TMA trimethylaluminum, BET Brunauer-Emmet-Teller

Table 3. Physical system parameters determined as a result of the experiments and modelling carried out in this work. Abbreviations in the column headings: Sym. – symbol, Val. – mean value, Unc. – uncertainty determined as a 95% confidence interval. For the parameters affected by the CNT diameter, two values are given, corresponding to $d_{\min}=13.79\pm0.31$ nm and $d_{\max}=27.10\pm0.76$ nm in the upper and lower row, respectively.

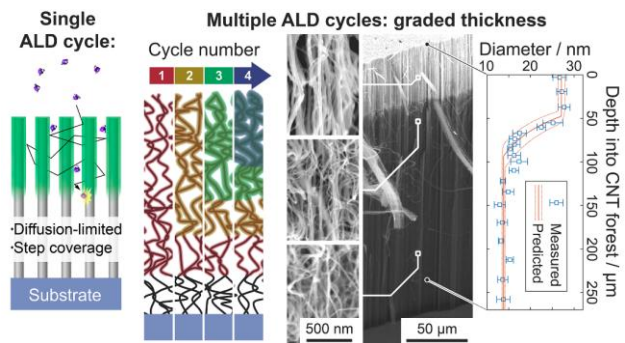
Parameter name	Sym.	Val.	Unc.	Unit
Surface area to volume ratio	α	18.7	± 2.4	$\frac{\mu\text{m}^2}{\mu\text{m}^3}$
		30.1	± 3.0	
Knudsen diffusivity	D	0.315	± 0.045	$\frac{\text{cm}^2}{\text{s}}$
		0.160	± 0.023	
Porosity	ε	0.933	± 0.010	-
		0.766	± 0.031	
Thiele number	h_T	132	± 23	-
		259	± 45	
Gas impingement rate onto nanostructure walls	J_{wall}	1.67	± 0.38	$\frac{10^{20}}{\text{cm}^2\text{s}}$
Knudsen number	Kn	79	± 13	-
		156	± 25	
Mean diffusion path until chemisorption ^v	λ_c	3.25	± 0.57	μm
		1.65	± 0.29	
Mean flight path confined by porous structure	λ_f	0.247	± 0.035	μm
		0.126	± 0.018	
Mean free path of TMA in bulk gas	λ_b	19.5	± 1.4	μm
Reactive site surface area	s_0	31.8	± 2.0	\AA^2
Pore wall surface area to pore volume ratio	\bar{s}	20.0	± 2.8	$\frac{\mu\text{m}^2}{\mu\text{m}^3}$
		39.4	± 5.5	
Mean diffusion time until chemisorption ^v	τ_c	168	± 42	ns
		85	± 21	
Mean flight time between subsequent molecule-wall collisions	τ_f	0.647	± 0.091	ns
		0.329	± 0.047	
Coating depth in a single cycle	z_c	94	± 14	μm
		47.7	± 7.4	

^v quantities determined assuming the sticking probability of TMA based on the results of Vandalon *et al.*⁴⁶

REFERENCES

- (1) George, S. M. Atomic Layer Deposition: An Overview. *Chemical Reviews* **2010**, *110* (1), 111–131. <https://doi.org/10.1021/cr900056b>.
- (2) Elam, J. W. Coatings on High Aspect Ratio Structures. In *Atomic Layer Deposition of Nanostructured Materials*; Pinna, N., Knez, M., Eds.; Wiley-VCH Verlag GmbH & Co. KGaA: Weinheim, Germany, 2012; pp 227–249.
- (3) Detavernier, C.; Dendooven, J.; Pulinthanathu Sree, S.; Ludwig, K. F.; Martens, J. A. Tailoring Nanoporous Materials by Atomic Layer Deposition. *Chemical Society Reviews* **2011**, *40* (11), 5242. <https://doi.org/10.1039/c1cs15091j>.
- (4) Keuter, T.; Menzler, N. H.; Mauer, G.; Vondahlen, F.; Vaßen, R.; Buchkremer, H. P. Modeling Precursor Diffusion and Reaction of Atomic Layer Deposition in Porous Structures. *Journal of Vacuum Science & Technology A* **2015**, *33* (1), 01A104. <https://doi.org/10.1116/1.4892385>.
- (5) Libera, J. A.; Elam, J. W.; Pellin, M. J. Conformal ZnO Coatings on High Surface Area Silica Gel Using Atomic Layer Deposition. *Thin Solid Films* **2008**, *516* (18), 6158–6166. <https://doi.org/10.1016/j.tsf.2007.11.044>.
- (6) Boukhalifa, S.; Evanoff, K.; Yushin, G. Atomic Layer Deposition of Vanadium Oxide on Carbon Nanotubes for High-Power Supercapacitor Electrodes. *Energy Environ. Sci.* **2012**, *5* (5), 6872. <https://doi.org/10.1039/c2ee21110f>.
- (7) Fisher, R. A.; Watt, M. R.; Konjeti, R.; Ready, W. J. Atomic Layer Deposition of Titanium Oxide for Pseudocapacitive Functionalization of Vertically-Aligned Carbon Nanotube Supercapacitor Electrodes. *ECS J. Solid State Sci. Technol.* **2015**, *4* (2), M1–M5. <https://doi.org/10.1149/2.0141502jss>.
- (8) Woo Kim, J.; Kim, B.; Won Park, S.; Kim, W.; Hyung Shim, J. Atomic Layer Deposition of Ruthenium on Plasma-Treated Vertically Aligned Carbon Nanotubes for High-Performance Ultracapacitors. *Nanotechnology* **2014**, *25* (43), 435404. <https://doi.org/10.1088/0957-4484/25/43/435404>.
- (9) Liang, Y.; Li, Y.; Wang, H.; Dai, H. Strongly Coupled Inorganic/Nanocarbon Hybrid Materials for Advanced Electrocatalysis. *J. Am. Chem. Soc.* **2013**, *135* (6), 2013–2036. <https://doi.org/10.1021/ja3089923>.
- (10) Eder, D. Carbon Nanotube–Inorganic Hybrids. *Chem. Rev.* **2010**, *110* (3), 1348–1385. <https://doi.org/10.1021/cr800433k>.
- (11) Vilatela, J. J.; Eder, D. Nanocarbon Composites and Hybrids in Sustainability: A Review. *ChemSusChem* **2012**, *5* (3), 456–478. <https://doi.org/10.1002/cssc.201100536>.
- (12) Deng, S.; Verbruggen, S. W.; He, Z.; Cott, D. J.; Vereecken, P. M.; Martens, J. A.; Bals, S.; Lenaerts, S.; Detavernier, C. Atomic Layer Deposition-Based Synthesis of Photoactive TiO₂ Nanoparticle Chains by Using Carbon Nanotubes as Sacrificial Templates. *RSC Adv.* **2014**, *4* (23), 11648. <https://doi.org/10.1039/c3ra42928h>.
- (13) Choi, T.; Kim, S. H.; Lee, C. W.; Kim, H.; Choi, S.-K.; Kim, S.-H.; Kim, E.; Park, J.; Kim, H. Synthesis of Carbon Nanotube–Nickel Nanocomposites Using Atomic Layer Deposition for High-Performance Non-Enzymatic Glucose Sensing. *Biosensors and Bioelectronics* **2015**, *63*, 325–330. <https://doi.org/10.1016/j.bios.2014.07.059>.
- (14) Nakashima, Y.; Ohno, Y.; Kishimoto, S.; Okochi, M.; Honda, H.; Mizutani, T. Fabrication Process of Carbon Nanotube Field Effect Transistors Using Atomic Layer Deposition Passivation for Biosensors. *J. Nanosci. Nanotech.* **2010**, *10* (6), 3805–3809. <https://doi.org/10.1166/jnn.2010.1983>.
- (15) Zhang, Y.; Guerra-Nuñez, C.; Utke, I.; Michler, J.; Rossell, M. D.; Erni, R. Understanding and Controlling Nucleation and Growth of TiO₂ Deposited on Multiwalled Carbon Nanotubes by Atomic Layer Deposition. *The Journal of Physical Chemistry C* **2015**, *119* (6), 3379–3387. <https://doi.org/10.1021/jp511004h>.
- (16) Acauan, L.; Dias, A. C.; Pereira, M. B.; Horowitz, F.; Bergmann, C. P. Influence of Different Defects in Vertically Aligned Carbon Nanotubes on TiO₂ Nanoparticle Formation through Atomic Layer Deposition. *ACS Appl. Mater. Interfaces* **2016**, *8* (25), 16444–16450. <https://doi.org/10.1021/acsami.6b04001>.
- (17) Stano, K. L.; Carroll, M.; Padbury, R.; McCord, M.; Jur, J. S.; Bradford, P. D. Conformal Atomic Layer Deposition of Alumina on Millimeter Tall, Vertically-Aligned Carbon Nanotube Arrays. *ACS Appl. Mater. Interfaces* **2014**, *6* (21), 19135–19143. <https://doi.org/10.1021/am505107s>.
- (18) Jensen, D. S.; Kanyal, S. S.; Madaan, N.; Miles, A. J.; Davis, R. C.; Vanfleet, R.; Vail, M. A.; Dadson, A. E.; Linford, M. R. Ozone Priming of Patterned Carbon Nanotube Forests for Subsequent Atomic Layer Deposition-like Deposition of SiO₂ for the Preparation of Microfabricated Thin Layer Chromatography Plates. *Journal of Vacuum Science & Technology B, Nanotechnology and Microelectronics: Materials, Processing, Measurement, and Phenomena* **2013**, *31* (3), 031803. <https://doi.org/10.1116/1.4801834>.
- (19) Cavanagh, A. S.; Wilson, C. A.; Weimer, A. W.; George, S. M. Atomic Layer Deposition on Gram Quantities of Multi-Walled Carbon Nanotubes. *Nanotechnology* **2009**, *20* (25), 255602. <https://doi.org/10.1088/0957-4484/20/25/255602>.
- (20) Guerra-Nuñez, C.; Zhang, Y.; Li, M.; Chawla, V.; Erni, R.; Michler, J.; Park, H. G.; Utke, I. Morphology and Crystallinity Control of Ultrathin TiO₂ Layers Deposited on Carbon Nanotubes by Temperature-Step Atomic Layer Deposition. *Nanoscale* **2015**, *7* (24), 10622–10633. <https://doi.org/10.1039/C5NR02106E>.
- (21) Wang, H.; Wei, M.; Zhong, Z.; Wang, Y. Atomic-Layer-Deposition-Enabled Thin-Film Composite Membranes of Polyimide Supported on Nanoporous Anodized Alumina. *Journal of Membrane Science* **2017**, *535*, 56–62. <https://doi.org/10.1016/j.memsci.2017.04.026>.
- (22) Ji, S.; Cho, G. Y.; Yu, W.; Su, P.-C.; Lee, M. H.; Cha, S. W. Plasma-Enhanced Atomic Layer Deposition of Nanoscale Yttria-Stabilized Zirconia Electrolyte for Solid Oxide Fuel Cells with Porous Substrate. *ACS Appl. Mater. Interfaces* **2015**, *7* (5), 2998–3002. <https://doi.org/10.1021/am508710s>.
- (23) Cremers, V.; Puurunen, R. L.; Dendooven, J. Conformality in Atomic Layer Deposition: Current Status Overview of Analysis and Modelling. *Applied Physics Reviews* **2019**, *6* (2), 021302. <https://doi.org/10.1063/1.5060967>.
- (24) Yanguas-Gil, A.; Elam, J. W. Self-Limited Reaction-Diffusion in Nanostructured Substrates: Surface Coverage Dynamics and Analytic Approximations to ALD Saturation Times. *Chem. Vap. Deposition* **2012**, *18* (1–3), 46–52. <https://doi.org/10.1002/cvde.201106938>.
- (25) Yanguas-Gil, A. Thin Film Growth in Nanostructured Materials. In *Growth and Transport in Nanostructured Materials*; SpringerBriefs in Materials; Springer International Publishing: Cham, 2017; pp 69–99. https://doi.org/10.1007/978-3-319-24672-7_4.
- (26) Szymt, W.; Guerra-Nuñez, C.; Dransfeld, C.; Utke, I. Solving the Inverse Knudsen Problem: Gas Diffusion in Random Fibrous Media. *Journal of Membrane Science* **2021**, *620*, 118728. <https://doi.org/10.1016/j.memsci.2020.118728>.
- (27) Knudsen, M. Die Molekularströmung der Gase durch Öffnungen und die Effusion. *Ann. Phys.* **1909**, *333* (5), 999–1016. <https://doi.org/10.1002/andp.19093330505>.

- (28) Knudsen, M. Die Gesetze der Molekularströmung und der inneren Reibungsströmung der Gase durch Röhren. *Annalen der Physik* **1909**, 333 (1), 75–130. <https://doi.org/10.1002/andp.19093330106>.
- (29) Dendooven, J.; Deduytsche, D.; Musschoot, J.; Vanmeirhaeghe, R. L.; Detavernier, C. Modeling the Conformality of Atomic Layer Deposition: The Effect of Sticking Probability. *Journal of The Electrochemical Society* **2009**, 156 (4), P63. <https://doi.org/10.1149/1.3072694>.
- (30) Dendooven, J.; Detavernier, C. Basics of Atomic Layer Deposition: Growth Characteristics and Conformality. In *Atomic Layer Deposition in Energy Conversion Applications*; Bachmann, J., Ed.; Wiley-VCH Verlag GmbH & Co. KGaA: Weinheim, Germany, 2017; pp 1–40. <https://doi.org/10.1002/9783527694822.ch1>.
- (31) Thiele, E. W. Relation between Catalytic Activity and Size of Particle. *Ind. Eng. Chem.* **1939**, 31 (7), 916–920. <https://doi.org/10.1021/ie50355a027>.
- (32) Gordon, R. g.; Hausmann, D.; Kim, E.; Shepard, J. A Kinetic Model for Step Coverage by Atomic Layer Deposition in Narrow Holes or Trenches. *Chem. Vap. Deposition* **2003**, 9 (2), 73–78. <https://doi.org/10.1002/cvde.200390005>.
- (33) Szmyt, W.; Vogel, S.; Diaz, A.; Holler, M.; Gobrecht, J.; Calame, M.; Dransfeld, C. Protective Effect of Ultrathin Alumina Film against Diffusion of Iron into Carbon Fiber during Growth of Carbon Nanotubes for Hierarchical Composites Investigated by Ptychographic X-Ray Computed Tomography. *Carbon* **2017**, 115, 347–362. <https://doi.org/10.1016/j.carbon.2016.12.085>.
- (34) Puurunen, R. L. Growth Per Cycle in Atomic Layer Deposition: Real Application Examples of a Theoretical Model. *Chemical Vapor Deposition* **2003**, 9 (6), 327–332. <https://doi.org/10.1002/cvde.200306266>.
- (35) Díaz, B.; Härkönen, E.; Światowska, J.; Maurice, V.; Seyeux, A.; Marcus, P.; Ritala, M. Low-Temperature Atomic Layer Deposition of Al₂O₃ Thin Coatings for Corrosion Protection of Steel: Surface and Electrochemical Analysis. *Corrosion Science* **2011**, 53 (6), 2168–2175. <https://doi.org/10.1016/j.corsci.2011.02.036>.
- (36) Philip, A.; Thomas, S.; Kumar, K. R. Calculation of Growth per Cycle (GPC) of Atomic Layer Deposited Aluminium Oxide Nanolayers and Dependence of GPC on Surface OH Concentration. *Pramana - J Phys* **2014**, 82 (3), 563–569. <https://doi.org/10.1007/s12043-014-0715-8>.
- (37) Lee, B.; Park, S.-Y.; Kim, H.-C.; Cho, K.; Vogel, E. M.; Kim, M. J.; Wallace, R. M.; Kim, J. Conformal Al₂O₃ Dielectric Layer Deposited by Atomic Layer Deposition for Graphene-Based Nanoelectronics. *Applied Physics Letters* **2008**, 92 (20), 203102. <https://doi.org/10.1063/1.2928228>.
- (38) Brunauer, S.; Emmett, P. H.; Teller, E. Adsorption of Gases in Multimolecular Layers. *J. Am. Chem. Soc.* **1938**, 60 (2), 309–319. <https://doi.org/10.1021/ja01269a023>.
- (39) Kim, J.; Chakrabarti, K.; Lee, J.; Oh, K.-Y.; Lee, C. Effects of Ozone as an Oxygen Source on the Properties of the Al₂O₃ Thin Films Prepared by Atomic Layer Deposition. *Materials Chemistry and Physics* **2003**, 78 (3), 733–738. [https://doi.org/10.1016/S0254-0584\(02\)00375-9](https://doi.org/10.1016/S0254-0584(02)00375-9).
- (40) Cheng, L.; Qin, X.; Lucero, A. T.; Azcatl, A.; Huang, J.; Wallace, R. M.; Cho, K.; Kim, J. Atomic Layer Deposition of a High-*k* Dielectric on MoS₂ Using Trimethylaluminum and Ozone. *ACS Appl. Mater. Interfaces* **2014**, 6 (15), 11834–11838. <https://doi.org/10.1021/am5032105>.
- (41) Carlsson, J.-O. Thermodynamics of the Homogeneous and Heterogeneous Decomposition of Trimethylaluminum, Monomethylaluminum, and Dimethylaluminumhydride: Effects of Scavengers and Ultraviolet-Laser Photolysis. *J. Vac. Sci. Technol. B* **1991**, 9 (6), 2759. <https://doi.org/10.1116/1.585642>.
- (42) Vass, G.; Tarczay, G.; Magyarfalvi, G.; Bödi, A.; Szepes, L. HeI Photoelectron Spectroscopy of Trialkylaluminum and Dialkylaluminum Hydride Compounds and Their Oligomers. *Organometallics* **2002**, 21 (13), 2751–2757. <https://doi.org/10.1021/om010994h>.
- (43) Bello, I. *Vacuum and Ultravacuum: Physics and Technology*, 1st ed.; CRC Press, 2017. <https://doi.org/10.1201/9781315155364>.
- (44) Ismail, A. F.; Khulbe, K. C.; Matsuura, T. Fundamentals of Gas Permeation Through Membranes. In *Gas Separation Membranes*; Springer International Publishing: Cham, 2015; pp 11–35. https://doi.org/10.1007/978-3-319-01095-3_2.
- (45) Shaeri, M. R.; Jen, T.-C.; Yuan, C. Y.; Behnia, M. Investigating Atomic Layer Deposition Characteristics in Multi-Outlet Viscous Flow Reactors through Reactor Scale Simulations. *International Journal of Heat and Mass Transfer* **2015**, 89, 468–481. <https://doi.org/10.1016/j.ijheatmasstransfer.2015.05.079>.
- (46) Vandalon, V.; Kessels, W. M. M. E. Initial Growth Study of Atomic-Layer Deposition of Al₂O₃ by Vibrational Sum-Frequency Generation. *Langmuir* **2019**, 35 (32), 10374–10382. <https://doi.org/10.1021/acs.langmuir.9b01600>.
- (47) Gakis, G. P.; Vergnes, H.; Scheid, E.; Vahlas, C.; Boudouvis, A. G.; Caussat, B. Detailed Investigation of the Surface Mechanisms and Their Interplay with Transport Phenomena in Alumina Atomic Layer Deposition from TMA and Water. *Chemical Engineering Science* **2019**, 195, 399–412. <https://doi.org/10.1016/j.ces.2018.09.037>.



Insert Table of Contents artwork here
